JOURNAL OF GEOPHYSICAL RESEARCH, VOL. 115, D00H20, doi:10.1029/2009JD012152, 2010



# Using CALIPSO to explore the sensitivity to cirrus height in the infrared observations from NPOESS/VIIRS and GOES-R/ABI

A. K. Heidinger,[1] M. J. Pavolonis,[1] R. E. Holz,[2] Bryan A. Baum,[3] and S. Berthier[2]

Received 31 March 2009; revised 28 October 2009; accepted 1 December 2009; published 29 April 2010.

[1] This paper demonstrates how the availability of specific infrared channels impacts the ability of two future meteorological satellite imagers to estimate cloud-top pressure. Both of the imagers are planned for launch by the United States, one for a geostationary platform and the other for a polar-orbiting platform. The geostationary imager, the Advanced Baseline Imager (ABI), will be flown first on the GOES-R platform. In addition to the split window channels at 11 and 12 $\mu$m, it has one spectral channel located at 13.3 $\mu$m where there is relatively strong absorption of $H_2O$ and $CO_2$. The polar-orbiting imager, called the Visible/Infrared Imager Radiometer Suite (VIIRS) and flown on the National Polar-Orbiting Environmental satellite Suite (NPOESS), has spectral channels in window regions only. The lack of an absorbing channel on VIIRS is shown to have negative consequences for the inference of cloud-top pressure. This paper investigates the impact on the ability of a satellite imager such as VIIRS to confidently estimate cloud-top pressure due to the absence of infrared absorption channels. The solution space is defined as the depth of the atmospheric layer in which a cloud can be placed where the calculated top-of-atmosphere radiances match the measurements used in the cloud-top pressure retrieval. For optically thin cirrus, the channels used by the operational VIIRS algorithm provide a solution space of over 200 hPa. However, the inclusion of the single $CO_2$ channel at 13.3 $\mu$m on the ABI narrows the solution space to under 30 hPa. Our imager-based analysis is performed using Moderate Resolution Imaging Spectroradiometer (MODIS) data, which provides the relevant channel information with sufficient spatial resolution and radiometric accuracy. Additional results are provided using data from the current GOES and POES imagers. Active lidar data from Cloud-Aerosol Lidar and Infrared Pathfinder Satellite Observation/Cloud-Aerosol Lidar with Orthogonal Polarization (CALIPSO/CALIOP) observations are used to provide cloud boundaries for verification.

**Citation:** Heidinger, A. K., M. J. Pavolonis, R. E. Holz, B. A. Baum, and S. Berthier (2010), Using CALIPSO to explore the sensitivity to cirrus height in the infrared observations from NPOESS/VIIRS and GOES-R/ABI, *J. Geophys. Res.*, *115*, D00H20, doi:10.1029/2009JD012152.

## 1. Introduction

[2] The future National Polar-Orbiting Environmental Satellite Suite (NPOESS) Visible and Infrared Imaging Radiometer Suite (VIIRS) will replace the current Polar-Orbiting Environmental Satellite (POES) Advanced Very High Resolution Radiometer (AVHRR) as the operational imager on the United States operational meteorological polar orbiting satellite platforms. The NPOESS paradigm represents a change in the design and procurement process of meteorological satellites. For NPOESS, the sensor and algorithms are designed and constructed by private industry to meet specifications requested by the formal users of the satellite data products. During the competitive phase of the procurement process, government scientists and engineers were not allowed to direct the design of either the algorithms or the sensors. One important decision made by the VIIRS design team was to exclude any infrared (IR) channels located in $H_2O$ or $CO_2$ absorption bands. This paper examines the consequences of that decision on the ability to estimate the cloud-top pressure for optically thin high cloud (i.e., cirrus). Unlike VIIRS, the GOES-R Advanced Baseline Imager was designed with a NOAA-specified channel set that included three $H_2O$ and one $CO_2$ infrared absorption bands [*Schmit et al.* 2005]. Another consequence of the lack of an IR absorption channel on VIIRS is the inability to track

[1]Center for Satellite Applications and Research, NESDIS, NOAA, Madison, Wisconsin, USA.
[2]Cooperative Institute for Meteorological Satellite Studies, University of Wisconsin-Madison, Madison, Wisconsin, USA.
[3]Space Science and Engineering Center, University of Wisconsin-Madison, Madison, Wisconsin, USA.

**Table 1.** Spectral and Radiometric Characteristics of MODIS Spectral Bands for Which Results are Shown in This Study

| MODIS Band | Wavelength Range ($\mu$m) | Similar VIIRS Channel | Similar GOES-R ABI Channel | Similar GOES-NOP Imager Channel | Similar AVHRR Channel | Principal Absorbing Components |
|---|---|---|---|---|---|---|
| 20 | 3.66–3.84 | M12 | 7 | 2 | 3b | $H_2O$, $CO_2$, $CH_4$ |
| 29 | 8.40–8.70 | M14 | 12 | | | $H_2O$, $O_3$, $SO_2$ |
| 31 | 10.78–11.28 | M15 | 14 | 4 | 4 | $H_2O$ |
| 32 | 11.77–12.27 | M16 | 15 | | 5 | $H_2O$, $CO_2$ |
| 33 | 13.185–13.485 | | | 6 | | $H_2O$, $CO_2$, $O_3$ |

water vapor features and derive atmospheric motion vectors, as demonstrated on MODIS by *Key et al.* [2003].

[3] The goal of this paper is to examine the consequences of the VIIRS and ABI channel selections on the estimation of cloud pressure for cirrus clouds, which can be problematic because such clouds are optically thin and infrared channels offer little contrast with clear-sky observations. Cirrus clouds are ubiquitous and their broadband radiative impact is in large part determined by their opacity and height (i.e., cloud-top pressure). In addition, cloud-top pressure products from imagers are beginning to be assimilated into numerical weather prediction (NWP) models and this effort will certainly expand in the ABI and VIIRS eras [*Bayler et al.*, 2000]. While the Cross-track Infrared Sounder (CrIS) on NPOESS will provide a wealth of infrared measurements in absorption bands, there are no baseline CrIS cloud products. In addition, CrIS observations are currently planned to be available on only one of the two NPOESS orbits. Therefore, continued research on the VIIRS cloud-top pressure performance is warranted.

[4] Our analysis will explore the inference of cloud-top pressure from the IR spectral information provided by the ABI and VIIRS channels in a way that is independent of the actual operational algorithms. Our focus is on exploring the spectral information content that will be available to a given imager pixel. Operational algorithms may attempt to overcome the spectral deficiencies through use of spatial and temporal information. In addition, optimal estimation techniques can be employed to improve the performance of cloud-top pressure estimates through the inclusion of a priori constraints from climatological data or other sources [*Heidinger and Pavolonis*, 2009]. The current operational VIIRS infrared cloud-top pressure algorithm is described by *Wong et al.* [2007] (referred to as W07). The operational algorithm from ABI is still under development although a working prototype has been developed within the GOES-R Algorithm Working Group (AWG) that uses the IR spectral channels described in this study.

## 2. Data and Models

[5] The Moderate Resolution Imaging Spectroradiometer (MODIS) channel set contains analogous versions of all of the infrared channels on VIIRS and all but one (10.4 $\mu$m) of the IR channels on the ABI. The mapping between the relevant channels on the VIIRS and GOES-R ABI to the analogous MODIS channels is given in Table 1. MODIS is a 36-band whiskbroom scanning radiometer currently in operation on the NASA Terra and Aqua platforms. The Aqua platform is part of the so-called A-Train [*Stephens et al.*, 2002], and was launched in May 2002. The Aqua platform is in an ascending orbit with a 1330 local crossing time. MODIS comprises four focal planes covering the spectral range 0.42–14.24 $\mu$m, with each spectral band defined by an interference filter. While the spatial resolution for nadir views varies from 250 m to 1 km, depending on the spectral band, all IR channels are at 1 km resolution. MODIS has several onboard instruments for in-orbit radiometric and spectral characterization. The IR spectral bands are calibrated with an onboard blackbody.

[6] Also used in this study is an active lidar called the Cloud-Aerosol LIdar with Orthogonal Polarization (CALIOP). The CALIOP instrument is on the CALIPSO satellite platform, which became part of the A-Train constellation in April 2006. The CALIPSO platform resulted from collaboration between NASA and the French space agency CNES, and began to collect data in June 2006. The mean altitude of the satellite is 705 km, and the lidar data have vertical and horizontal resolutions of 30 and 330 m, respectively.

[7] The VIIRS approach outlined in W07 uses channels with central wavelengths of approximately 3.75, 8.5, 11 and 12 $\mu$m, which corresponds to MODIS channels 20, 29, 31 and 32. The proposed ABI approach uses channels with central wavelengths of 11, 12 and 13.3 $\mu$m which corresponds to MODIS channels 31, 32, and 33. Throughout this analysis, only the MODIS channel numbers will be used in the description of the results. For example channel 31 will be denoted as ch31 and these quantities will always refer to the equivalent blackbody brightness temperature unless stated otherwise. Figure 1 shows the relevant MODIS spectral response functions overlaid on a spectrum of nadir transmission computed for a clear standard Tropical atmosphere using MODTRAN4 [*Anderson et al.*, 2000].

[8] A large part of this analysis requires the use of clear-sky radiative transfer calculations. The clear-sky radiative transfer model (RTM) used here was the Pressure-layer Fast Algorithm for Atmospheric Transmittances (PFAAST) model provided by Hal Woolf from the University of Wisconsin and is described by *Hannon et al.* [1996]. The RTM was driven by atmospheric profiles from the National Center for Environmental Prediction (NCEP) Global Forecast System (GFS) 12 h forecasts. The NCEP data were temporally interpolated between the surrounding 6 h model cycles to the mean time for each MODIS granule. The RTM was called at the spatial resolution of the NWP data (0.5 deg). The RTM was called multiple times within each cell to ensure that angular differences between the MODIS observations and the RTM calculations were less than 0.01 in cosine of viewing zenith angle. The surface emissivity used in computing the TOA radiance values for each pixel was taken from the spectrally resolved 5 km global surface emissivity database described by *Seemann et al.* [2008].

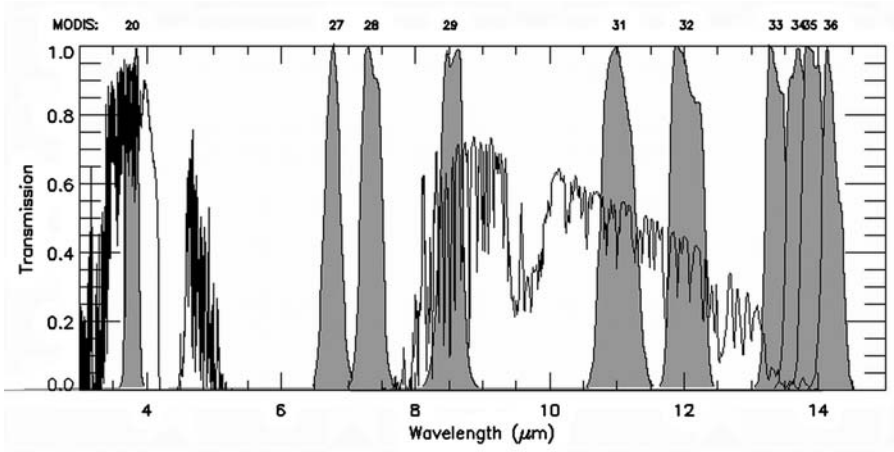


**Figure 1.** Response functions of MODIS channels used for cloud height retrieval. Response functions are shown as gray shapes overlaid on a nadir transmission spectrum computed for a standard tropical atmosphere. NPOESS/VIIRS provides channels similar to MODIS channels 20, 29, 31, and 32. GOES-R/ABI provides channels similar to MODIS channels 20, 29, 31, 32, and 33.

[9] The data used in this study come from the intersection of CALIPSO/CALIOP and AQUA/MODIS data for a 5 min granule (2035–2040 UTC, 10 August 2006) that was recorded over the Indian Ocean at roughly 2 h after local midnight. The goal of this work is to relate the available IR spectral information to the sensitivity to cloud-top pressure. The chosen granule is useful in illuminating this sensitivity as it entails a large-scale cirrus cloud of varying opacity. Our analysis of other scenes indicates that the features of this analysis are robust and thus are not overly dependent on the properties of the cirrus and of the underlying surface.

[10] Figures 2, 3, and 4 provide the MODIS and CALIPSO views of this granule. Figure 2 shows a MODIS false color image with the CALIPSO track overlaid in red. In this image, only the 250 MODIS pixels surrounding the CALIPSO track are shown. The false color image is created with the red image being the ch20–ch31 brightness temperature difference (BTD [3.75–11]), the green image being the ch31–ch32 brightness temperature difference (BTD[11–12]) and the blue image being the ch31 brightness temperature (BT11) gray-flipped so that lower temperatures result in higher intensities. In this color combination, cirrus clouds appear white but as the optical thickness increases, the ice clouds appear as light blue/cyan. Low-level water clouds appear as dark blue, and midlevel water clouds tend to have a red/orange color. Figure 3 shows the 532 nm total backscattering image generated from the v2.01 level 1b CALIPSO/CALIOP data from the NASA Langley Research Center. Figure 4 shows a cross section along the CALIPSO track of the MODIS ch31 brightness temperature (black line), the highest cloud midlayer temperature from CALIOP (red) and the calculated top-of-atmosphere (TOA) clear-sky ch31 brightness temperature. The green points in Figure 4 (bottom) are the derived 11 $\mu$m cloud emissivity values assuming the cloud emission occurs at the CALIOP midlayer temperature (red points). The estimation of cloud emissivity is accomplished through use of equation (1) and by setting the cloud pressure level to that provided by CALIOP. As Figure 3 indicates, the

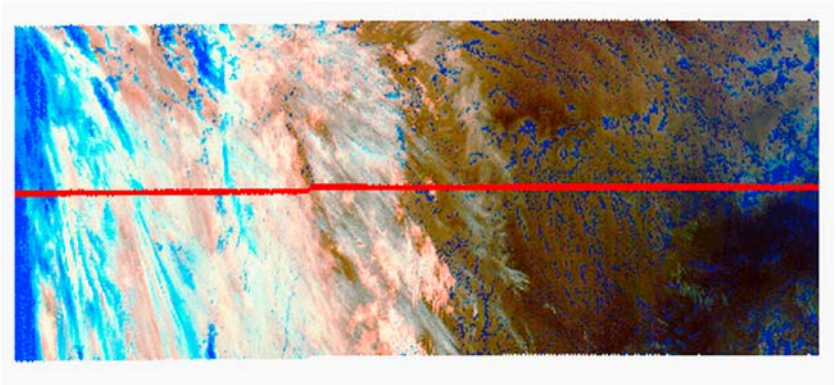

**Figure 2.** A false color image constructed from ch31–ch32 (red), ch20–ch31 (green), and ch31 reversed (blue). Data are taken from AQUA/MODIS and CALIPSO/CALIOP on 10 August 2006 from 2035 to 2040 UTC. The red line is the CALIPSO track. In this color combination, cirrus clouds appear white, but as the optical thickness increases, the ice clouds appear as light blue/cyan. Low-level water clouds appear as dark blue, and midlevel water clouds tend to have a red/orange color.

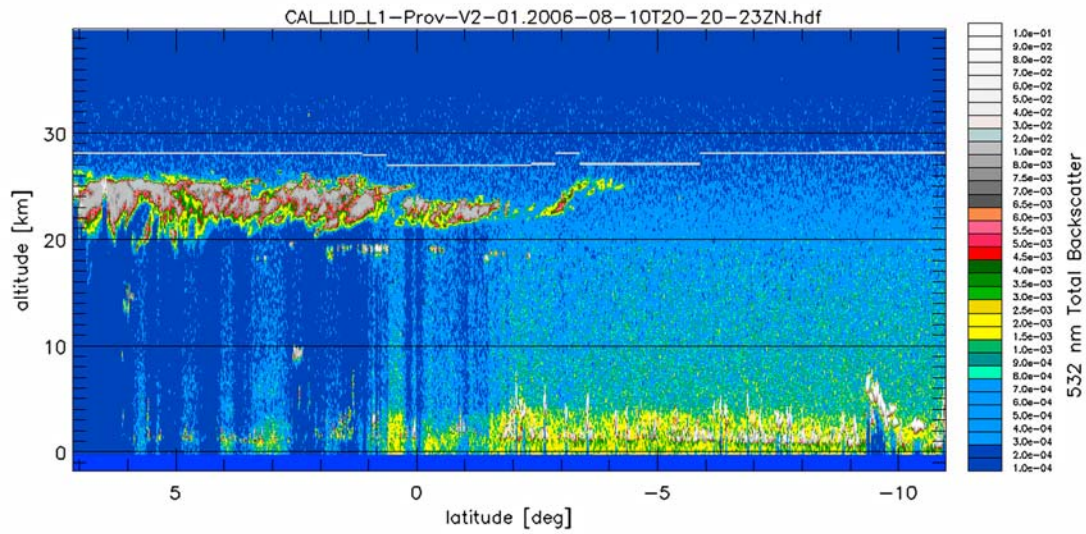


**Figure 3.** The 532 nm total backscatter from CALIOP along the red line shown in Figure 2. The gray horizontal line is the tropopause.

MODIS-CALIOP collocated data are characterized primarily by single-layer cirrus clouds that decrease in opacity as viewed from north to south. The CALIOP cloud layer products indicate that 82% of the cloudy pixels are classified as single layer for this scene. The most southern parts of the granule are free of cirrus. As shown later, the major driver of the cloud-top pressure performance is the cloud emissivity. Because this data set spans a wide range of cirrus cloud emissivity, it offers an ideal test bed for illustrating the spectral information content and the inference of the cloud-top pressure for the VIIRS and ABI channel combinations.

## 3. Analysis

[11] As stated earlier, the goal of this paper is to employ an analysis that focuses on the consequences of the spectral content, not on the details of any particular algorithm. While the results of this study represent the fundamental physical drivers of cloud-top pressure performance, we are not predicting the performance of the anticipated operational VIIRS or ABI products. The analysis used here is performed in terms of the cloud-top pressure solution space. The solution space is defined as the region of the atmosphere where a cloud can exist and where calculated radiances/brightness temperatures can reproduce the relevant observations to a given accuracy. A deep solution space means that the channels provide little skill in estimating a definitive value of cloud-top pressure. A narrow solution space means that the channels provide a high sensitivity to cloud-top pressure and can confidently estimate the cloud-top pressure within a small region of the atmosphere. We will express the solution space in the units of pressure (hPa) but this work could easily

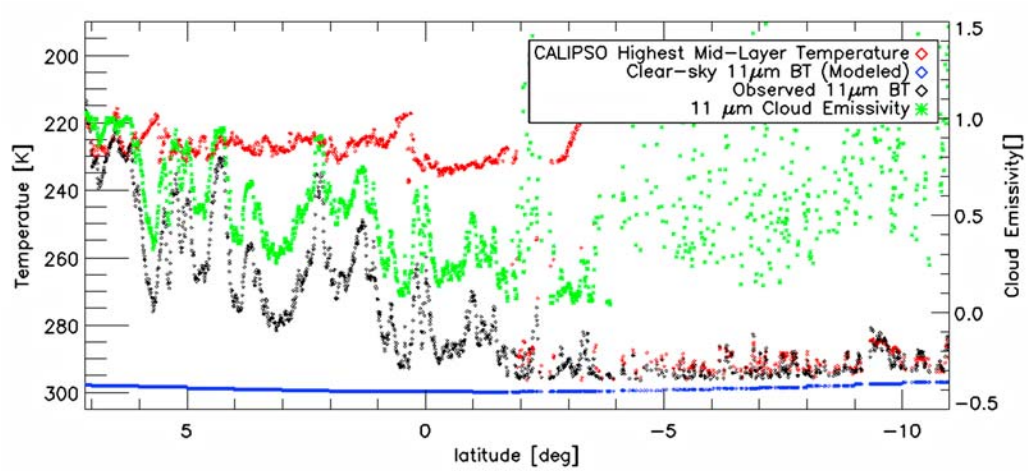


**Figure 4.** A cross section along the CALIPSO track of the observed ch31 BT (black), the computed clear-sky ch31 BT (blue), and CALIOP midlayer temperature for the highest cloud layer (red). The green points are the derived ch31 cloud emissivity assuming the cloud resided at the level determined by CALIOP. The data used for this image are taken along the red line in Figure 2 and the CALIOP data shown in Figure 3.

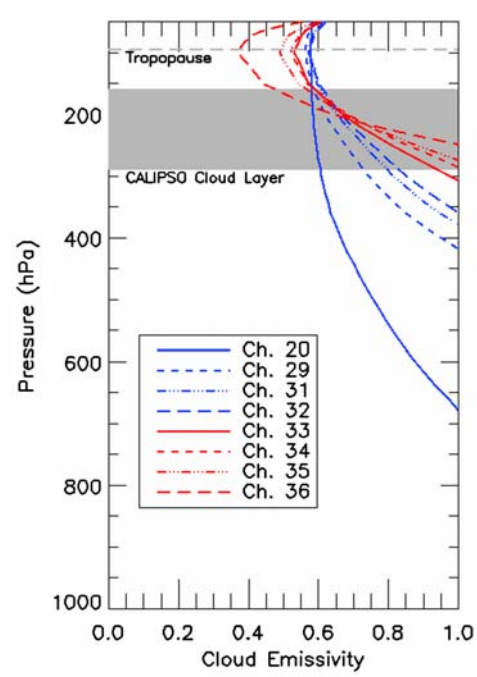


**Figure 5.** Profiles of cloud emissivity in several channels for one pixel along the CALIPSO track. CALIOP-derived ch31 emissivity was approximately 0.60. The cloud emissivities are computed by using equation (1). The blue lines show the profiles for the various window channels used in this study. The red lines show the profiles for the long-wave $CO_2$ channels (ch33–ch36). The boundaries of the cloud as determined by CALIOP are shown as the gray region.

express the solution space in the units of height (km) or temperature (K).

[12] To demonstrate the analysis developed here, a single pixel from Figure 4 was chosen. It was chosen based on its 11 $\mu$m cloud emissivity value (0.6), which is close to global mean value for cirrus given by *Heidinger and Pavolonis* [2009]. Figures 5, 8, 9 and 10 show profiles generated for this pixel to illustrate the methodology that will be employed to all cirrus pixels.

### 3.1. Cloud Emissivity Profiles

[13] The first step in the analysis is to compute profiles of cloud emissivity for each relevant channel. A cloud emissivity profile can be computed using the following relation:

$$e_c^{(p)} = {(I - I_{clr})}\Big/{(I_{ac}(p) + \mathrm{T}_{ac}(p) I_{bb}(p) - I_{clr})}. \quad (1)$$

In equation (1), I is the observed TOA radiance, $I_{clr}$ is the simulated TOA clear-sky radiance, $I_{ac}(p)$ is the simulated above-cloud emission, $T_{ac}(p)$ is the simulated above-cloud transmission and $I_{bb}(p)$ is the simulated TOA radiance from a blackbody cloud emitting at the temperature of the pressure level associated with value of pressure denoted as $p$. The channel dependence in equation (1) is implicit and is not shown. In equation (1), the cloud is modeled as a vertically homogenous isothermal layer. The cloud-top temperature is therefore physically the effective emission temperature of the cloud, which corresponds to a level below the cloud top. The effects of scattering between the cloud, atmosphere and surface are totally ignored in equation (1). The effect of in-cloud scattering is approximated as described later by treating the cloud emissivity as an effective emissivity and including scattering in the $\beta$ values defined later in equation (3). Approximations of scattering are common and appropriate in models of top-of-atmosphere infrared window observations where transmission through the cloud is the dominant driver of the radiative transfer.

[14] All levels where $e_c(p)$ falls between 0 and 1, represent levels where a cloud can exist and match the observed radiance in the chosen channel. The cloud emissivity profile therefore represents the solution space offered by a single channel. It provides a merger of the information from the sensor with information from the clear-sky RTM. Figure 5 shows the cloud emissivity profiles computed for the chosen pixel for all of the relevant channels on VIIRS and ABI. For reference, the tropopause level and the boundaries of the cloud as determined by CALIOP are shown in Figures 5, 8, 9 and 10. For the window channels (ch20, ch29, ch31 and ch32) the relative variation in the emissivity profiles is a function of the spectral variation of cloud opacity. In general, the cloud optical thickness increases for cirrus cloud going from ch20, ch29, ch31 and ch32 and this seen in relative distribution of the cloud emissivity profiles. The deepest single-channel solution space is offered by ch20 and the narrowest by ch32. For the channel on the edge of $CO_2$ absorption band, ch33, the emissivity profile is affected by gaseous absorption. Channels with large amounts of gaseous absorption are weakly influenced by the surface and lose all ability to detect clouds below some level. Though ch33 is a relatively weak $CO_2$ absorbing channel, the presence of $CO_2$ does significantly impact the emissivity profile for this pixel as shown in Figure 5.

### 3.2. Cloud $\beta$ Profiles

[15] The emissivity profiles shown in Figure 5 show the solution space, as we have defined it, provided by each channel acting alone. To narrow that solution space further, algorithms employ multiple channels. To relate the emissivity profiles from multiple channels, we use the $\beta$ parameter that has been employed often in split-window infrared cloud remote sensing [*Parol et al.*, 1991]. The $\beta$ profiles can be computed from the emissivity profiles by

$$\beta_{x,y}(p) = {\ln\left(1 - e_{c,y}(p)\right)}\Big/{\ln\left(1 - e_{c,x}(p)\right)}. \quad (2)$$

In equation (2), x and y refer to the two channels used to compute the ratio. $\beta$ is a useful parameter because it provides a direct link from observed quantities to the single scattering properties. As provided by *Parol et al.* [1991], $\beta$ is well approximated by the following relation

$$\beta_{x,y} \approx {\left((1 - \omega_{o,y} g_y) Q_{ext,y}\right)}\Big/{\left((1 - \omega_{o,x} g_x) Q_{ext,x}\right)}, \quad (3)$$

where $\omega_o$ is the single scatter albedo, $g$ is the asymmetry parameter and $Q_{ext}$ is the extinction efficiency. For the strongly absorbing channels used in this study, $\beta$ is often approximated by the ratio of the absorption optical depths at

the two channels. As shown by *Parol et al.* [1991], however, the absorption-only $\beta$ values can differ significantly from the values given by (3) for calculations at 11 and 12 $\mu$m. Parol et al. refer to values in (3) as effective $\beta$ values and this definition is used throughout this study.

[16] Since $\beta$ is directly related to the single scattering properties through equation (3), it can be directly related to particle size once an assumption of particle habit and composition is made. For this analysis, we assume that the cirrus cloud particles can be modeled as aggregates and that the scattering properties are those provided by *Yang et al.* [2005]. In the Yang database, the effective radii are defined as the 0.75 times the ratio of the integrated volume divided by the projected area.

[17] The Yang database provides properties for 7 habits. Because some studies have shown that aggregates are an appropriate choice for the modeling of some cirrus clouds [*Fu and Sun*, 2001], we have chosen to model the clouds here as having the scattering properties of aggregates from the Yang database. Further testing (not shown) has shown that the relative cloud-top pressure solution space results of this analysis are not highly dependent on the chosen habit. However, the derived cloud effective radii do show a significant sensitivity to the assumed cloud microphysical assumptions.

[18] Another option is to use the habit mixtures suggested by *Baum et al.* [2005] which are derived from the Ping Yang database and are used in the MODIS Collection 5 cloud optical and microphysical products. In addition, ice scattering properties could also be generated using the modified anomalous diffraction approximation (MADA) where ice particles are described by their mass- and projected area–dimension power law relationships [*Jensen et al.*, 2009].

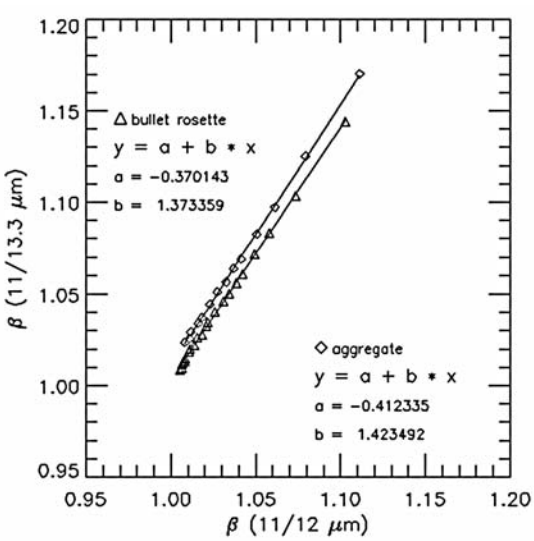


**Figure 6.** Variation in $\beta$ derived from ch32 and ch29 compared with that from $\beta$ derived from ch31 and ch20. The $\beta$ is defined using equation (3) based on the scattering properties predicted for aggregate and bullet rosette ice crystals provided by *Yang et al.* [2005]. These channel combinations are used in the *Wong et al.* [2007] VIIRS cloud height algorithm.

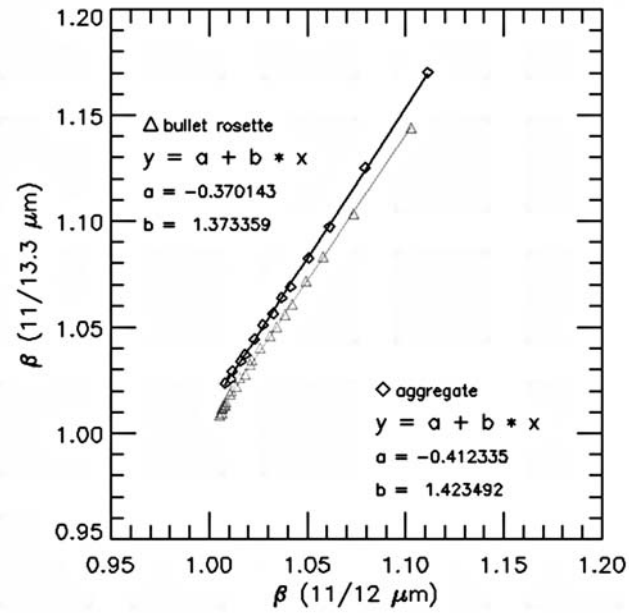


**Figure 7.** Variation in $\beta$ derived from ch31 and ch33 compared with that from $\beta$ derived from ch31 and ch32. The $\beta$ is defined using equation (3) based on the scattering properties predicted for aggregate and bullet rosette ice crystals provided by *Yang et al.* [2005]. These channel combinations are being proposed for use in a GOES-R/ABI cloud height algorithm.

[19] Once the decision is made to model cirrus as comprising aggregates as provided by *Yang et al.* [2005], we can predict the variation of $\beta$ between various channel combinations. Figure 6 shows the predicted variation in $\beta$ from two different channel pairs used in the VIIRS algorithm and Figure 7 shows the predicted variation in $\beta$ from the two channel pairs used in the GOES-R/ABI algorithm. The $\beta$ values are computed from the Yang database by assuming a monodisperse size distribution (single size) and integrating spectrally over the MODIS channel response functions. The $\beta$ calculations performed assuming monodisperse size distributions compare well to those computed using the monomodal size distributions and habit mixtures used in the ice model developed by *Baum et al.* [2005] which are derived from the Yang database. The sensitivity of $\beta$ in the presence of multimodal distributions has not been determined. The linear regressions shown in Figure 6 and Figure 7 are used later when the cloud-top solution space is predicted from multiple channel pairs.

## 4. Definition of Cloud-Top Pressure Solution Space

[20] Figure 8 shows the $\beta$ profiles derived from the emissivity profiles shown in Figure 5 using equation (2) for the channels used in the VIIRS approach (W07). While the W07 algorithm is cast in term of $k$ ratios, where $k$ is the mass absorption coefficient for ice, $k$ ratios themselves are closely related to the $\beta$ parameters. As formulated in W07, the $k$ ratios are actually $\beta$ parameters computed assuming no scattering.

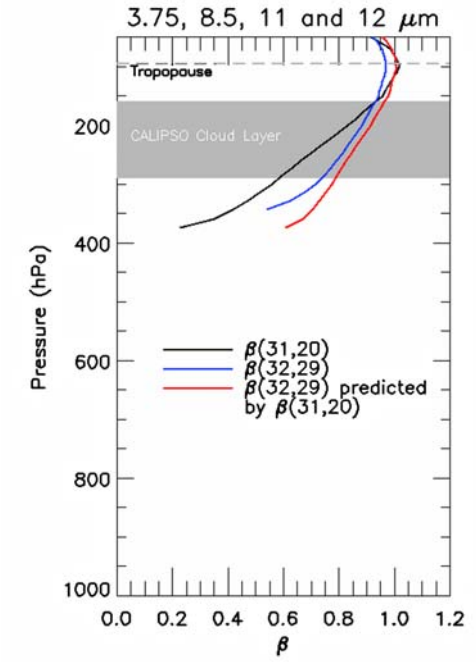


**Figure 8.** Profiles of $\beta$ computed from emissivity profiles using equation (2). The black line shows the observed $\beta$(31,20) profile while the blue line shows the observed $\beta$(32,29) profile. The red curve is the $\beta$(32,29) profile predicted from the black curve and the linear regression given in Figure 4. The region where the red and blue curves intersect gives the solution space provided by this channel combination. The solution space refers to the region where a cloud can be placed at match all of the observations used in computing it. The channel set shown here is provided by NPOESS/VIIRS.

The W07 algorithm uses $\beta$ values derived from ch29 and ch32 and from ch20 and ch31. We adopt the same channel pairs for this analysis. We denote $\beta$(29,32) as the $\beta$ value derived from ch29 and ch32 which is referred to as k12/k15 in W07. Correspondingly, we denote $\beta$(20,31) as $\beta$ value derived from ch20 and ch31 which is referred to as k14/k15 in W07. In Figure 8, the $\beta$(31,20) profile is shown as the black line and the $\beta$(32,29) profile is shown as the blue curve.

[21] As the emissivity profiles define the solution space for a single channel, the $\beta$ profiles define the solution space for a given channel pair. The cloud-top pressure solution space for a channel pair is defined as the region where both channel emissivities are valid (0–1) and the $\beta$ values fall within the expected range. For example, the use of the aggregate predicts that $\beta$(31,20) should range between 0.65 and 0.94 for particles with radii between 10 and 100 microns. Application of this to the $\beta$(31,20) profile in Figure 8 results in a solution space that spans approximately 280 to 170 hPa. Similarly, use of the aggregate predicts that $\beta$(32,29) should range from 0.67 to 0.9 for particles with radii between 10 and 100 $\mu$m. If this particle size range encompasses the expected range, the $\beta$(32,29) solution space will span from 320 to 210 hPa.

[22] In comparison with the emissivity profiles in Figure 5, these $\beta$ profiles do not offer a significant narrowing of the solution space. One could also explore the solution space provided by using multiple channel pairs. In this case, the solution space is defined as the region where all emissivities are valid and the two $\beta$ curves follow the relationships predicted by scattering theory. The $\beta$ profiles for the VIIRS channel set are shown in Figure 8. Based on scattering theory, we found that a simple linear relationship can approximate the variation of $\beta$(32,29) with $\beta$(31,20) as indicated in Figure 6. Therefore, $\beta$(32,29) can be predicted using the $\beta$(31,20) profile and the assumed linear relationship. The levels at which the predicted and observed $\beta$(32,29) profiles agree define the solution space; within the solution space, TOA radiances calculated for a cloud at any level will match the observations within the context of the assumed aggregate microphysical model. The predicted $\beta$(32,29) curve is shown as the red line in Figure 8. As Figure 8 shows, the predicted (red) and observed (blue) $\beta$(32,29) curves agree over the region between the tropopause and roughly 250 hPa which defines the solution space for these channels given the observed radiances. The result is that a cloud composed of aggregates can be placed at any level between the tropopause and 250 hPa and can reproduce the relevant MODIS observations.

[23] In contrast, the Figure 9 shows the $\beta$ profiles generated from the three channels (31, 32 and 33) being considered for a GOES-R/ABI cloud-top pressure algorithm. As was the case with the VIIRS channels, one can estimate the solution space provided by each channel pair by looking at where the $\beta$ values fall within a reasonable range as dictated by the assumed cloud microphysics. Use of the aggregate particle leads to a prediction that $\beta$(31,32) will range between 1.03 and 1.3 for particles with radii between 10 and 100 $\mu$m. Similarly, for $\beta$(31,33), values will range between 1.1 and

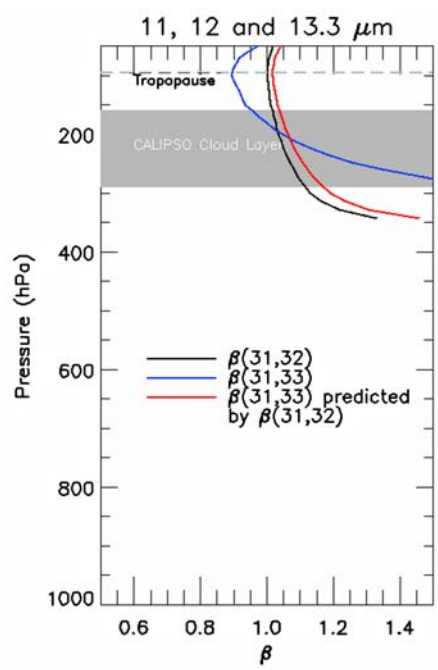


**Figure 9.** Same as Figure 6 but for the $\beta$(31,20) and $\beta$(31,33) profiles. These channel pairs are offered by the GOES-R/ABI.

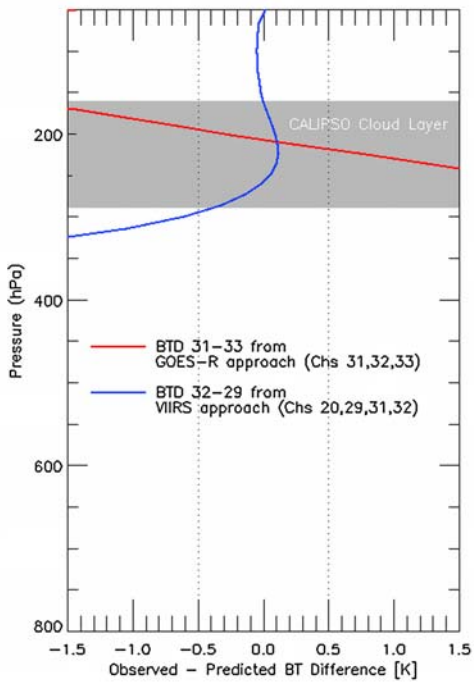


**Figure 10.** Profiles of the observed minus predicted brightness temperature difference (BTD) consistent with observed minus predicted $\beta$ profiles in Figures 8 and 9. For reference, the lines corresponding to ±0.5 K difference are shown. In this analysis, the region where the observed minus predicted BTD is with 0.5 K is assumed to define the solution space. The gray region shows the CALIOP cloud boundaries for this pixel.

1.4 for the same radii range. While the $\beta$(31,32) profile provides a solution space between 225 and 335 hPa, the $\beta$(31,33) profiles provide a solution space between 220 and 265 hPa.

[24] As with VIIRS, the ABI channel combinations can be used together to define a final solution space using channels 31, 32 and 33. To do this, we again the aggregate particle to predict the $\beta$(31,33) profile from the observed $\beta$(31,32) profile (black line). In Figure 9, the observed $\beta$(31,33) profile is shown as the blue line while the predicted $\beta$(31,33) is shown as the red line. Unlike Figure 8, where the predicted and observed $\beta$ profiles agree over a large region, the observed (blue) and predicted (red) $\beta$(31,33) agree over a much smaller region (i.e., they intersect). This behavior is caused by the inclusion of ch33 into the channel set. The absorption in ch33 causes the $\beta$(31,33) profile to have a slope that cannot be predicted by a linear translation of the $\beta$(31,32) profile. Therefore the predicted and observed profiles agree only in the vicinity where they cross each other, resulting in a much narrower solution space than seen in Figure 8.

[25] It is important to note the results of the paper do not account for any errors in the clear-sky pixel-level radiative transfer. Errors in the surface temperature, surface emissivity and atmospheric profiles can manifest themselves as errors in the estimated cloud-top pressure solution space. As described earlier, the data used here occur over the ocean where our knowledge of surface temperature and surface emissivity at these wavelengths is very accurate. It is also assumed that the errors in the short-term NWP forecast profiles are minimal and can be neglected. The final assumption is that our knowledge of the spectral response functions of the channels used in this study is sufficient to guarantee that the clear-sky forward model errors are negligible.

### 4.1. Computation of the Cloud-Top Pressure Solution Space for NPOESS/VIIRS and GOES-R/ABI

[26] In section 4, the cloud-top pressure solution space was defined as the vertical levels where the predicted and observed $\beta$ profiles used in a cloud-top pressure algorithm were in agreement. For computational ease and improved physical understanding, the actual computation of the solution space was accomplished using a radiometric definition. Solution spaces are therefore computed by applying a threshold on the difference between the observed and predicted brightness temperature differences (BTD) for same channel pair used to define the $\beta$ profile. As noted by *Heidinger and Pavolonis* [2009], the mean bias between computed and observed ch31–ch32 for the NOAA/AVHRR is about 0.5 K over land and 0.05 K over ocean. Based on this study, we have chosen a value of 0.5 K as a reasonable measure of our ability to simulate observed brightness temperature differences in the presence of cirrus. This value is also roughly twice the value of the instrument noise in each channel. Increasing this threshold has little impact on the results and decreasing this threshold has little impact on the relative performance of each channel set.

[27] Figure 10 shows an example BTD profile computed for the pixel used in computing the profiles in Figures 5, 8 and 9. The gray region illustrates the CALIPSO-derived cloud boundaries for reference. The dashed vertical lines define the region where the BTD differences were less than the chosen threshold (0.5K). The blue line in Figure 10 shows the ch29–ch32 BTD difference profile. Again, this profile is the difference in the TOA BTD observed with that computed by placing a cloud at each level with a $\beta$(32,29) value predicted by the observed $\beta$(31,20) value and the observed ch32 cloud emissivity value. This analysis ensures that every point on the blue curve automatically represents a cloud that matches the ch31–ch20 BTD.

[28] The red curve in Figure 10 provides the ch31–ch33 BTD (observed – predicted) profile computed for the same pixel. In this computation, the $\beta$(31,33) profile is computed from the observed $\beta$(31,32) profile and the observed $e_c$(31) profile. The important feature of Figure 10 is the slope of the red and blue curves. While the red curve (GOES-R) falls within the 0.5 K threshold for region roughly between 200 and 220 hPa, the blue curve (VIIRS) falls within the 0.5 K threshold for much broader region extending from 290 hPa to the tropopause (the assumed physical limit). Therefore for this pixel, the GOES-R channel set cloud-top pressure solution space is 20 hPa compared to 190 hPa for the VIIRS channel set. The curve that produces a zero BTD represents the optimal guess of the cloud level from this analysis where both channel sets give a value within the cloud. However, the cloud-top pressure solution space indicates that the uncertainty of using the GOES-R channel set is much less than that offered by the VIIRS channel set.

[29] Figure 11 shows the same analysis applied above to one pixel applied to all ice cloud pixels in the CALIPSO/AQUA cross section seen in Figures 2–4. The black symbols

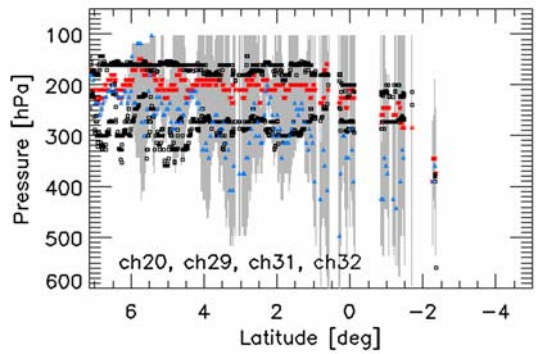


**Figure 11.** Cloud-top pressure solution space provided by the VIIRS IR channel set for the ice clouds along the CALIPSO track for 10 August 2006, 2035–2040 UTC. The gray lines represent the solution space provided by the selected IR channels. The black symbols provide the CALIOP cloud boundaries for the highest cloud layer. The red points provide the MYD06 values as a reference. The blue points represent the location of the optimal cloud-top pressure solutions with this channel set. For clarity, only every fifth optimal cloud-top pressure solution is plotted.

in Figure 11 show the CALIPSO-derived cloud boundaries. For reference, the red symbols provide the cloud-top pressure values from the Collection 5 AQUA/MODIS cloud product (MYD06). The cloud-top pressure solution space using the VIIRS channel set is shown by vertical gray lines. Each pixel generates one vertical gray line. As Figure 11 shows, the cloud-top pressure solution space varies from near zero to over 400 hPa. The blue points in Figure 11 represent the location of the optimal cloud-top pressure solutions with this channel set. The optimal cloud-top pressure is defined as the cloud vertical position where the observations match most closely. In contrast, Figure 12 shows the cloud-top solution space computed using the GOES-R channel set. In Figure 12, the cloud-top solution space varies from near zero to approximately 100 hPa.

[30] Both Figures 11 and 12 show a large spatial variability in the derived cloud-top pressure solution space. One would expect that this variability is driven by the cloud emissivity with the largest solution spaces occurring in the

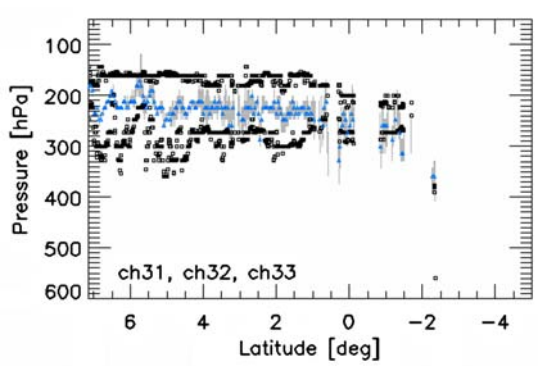


**Figure 12.** Same as Figure 11 but for the GOES-R/ABI IR channel set (31, 32, 33).

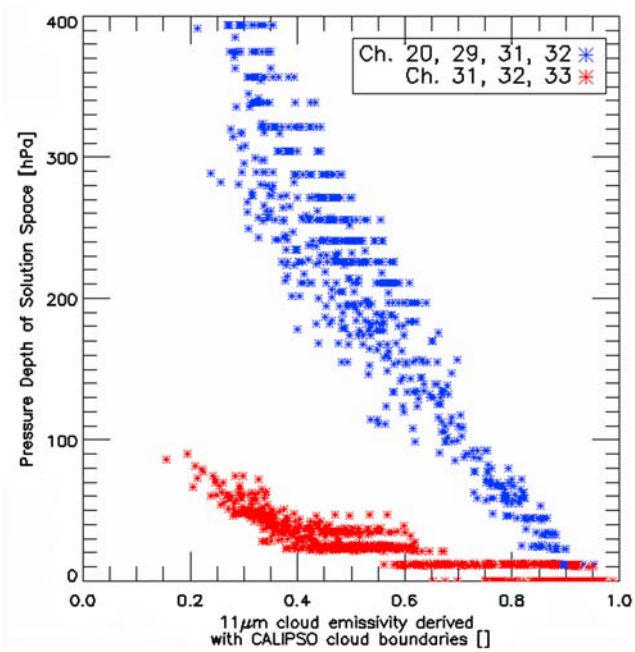


**Figure 13.** Correlation of the cloud-top pressure solution space provided by the NPOESS/VIIRS and GOES-R/ABI channel set with the derived 11 $\mu$m cloud emissivity using the MODIS/AQUA 11 $\mu$m observation and the CALIOP cloud temperature. The data are the same as those shown in Figures 11 and 12.

optically thinnest portions of the cloud. Figure 13 shows the variation of the cloud-top pressure solution space with the CALIPSO-derived cloud emissivity and confirms that the solution space increases with decreasing emissivity. Based on Figure 11, the VIIRS channel set solution space is roughly 200 hPa deep for clouds with emissivities around 0.5 while for the same clouds, the GOES-R channel set has a solution space approximately 25 hPa deep. For reference, Table 2 provides values of the solution space for GOES-R and VIIRS channel sets averaged for clouds with all values of emissivity, clouds with emissivities between 0.45 and 0.55 and clouds with emissivities between 0.15 and 0.25. Also given in Table 2 are the values of the cloud-top pressure solution space provided by ch29, ch31 and ch32.

### 4.2. Cloud-Top Solution Space Offered By Channels 29, 31, and 32 (VIIRS Climate)

[31] The baseline VIIRS algorithm described by W07 uses ch20, ch29, ch31 and ch32. Because ch20 has a significant solar component, the baseline VIIRS approach is applied

**Table 2.** Mean Solution Spaces

| | Cloud-Top Pressure Solution Space (hPa) | | |
|---|---|---|---|
| Channel Set | $0 < e_c < 1$ | $0.45 < e_c < 0.55$ | $0.15 < e_c < 0.25$ |
| 20, 29, 31, 32 | 205 | 240 | 438 |
| 31, 32 | 150 | 186 | 243 |
| 29, 31, 32 | 173 | 197 | 267 |
| 31, 33 | 49 | 56 | 94 |
| 31, 32, 33 | 27 | 26 | 84 |

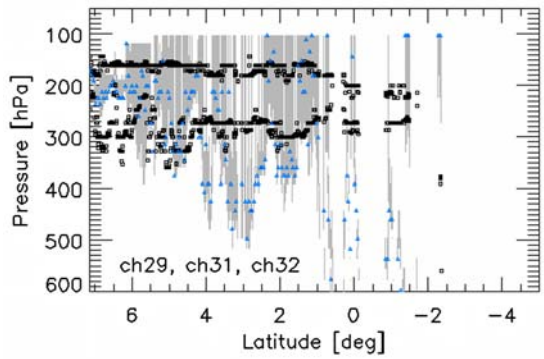


**Figure 14.** Same as Figure 11 but for the VIIRS climate IR channel set (29, 31, 32).

only at night and another approach that employs solar reflectance channels is used during the day. For climate applications, it is advantageous to employ methods that provide consistent results regardless of solar illumination. In this section, we explore the performance of the three-channel algorithm (denoted here as VIIRS climate) that uses ch29, ch31 and ch32 and thereby avoids any solar contribution. Figure 14 provides a visual measure of the cloud-top pressure solution space for the VIIRS climate channel set. In comparison to Figure 11, the VIIRS climate results are an improvement over the VIIRS results. Table 2 provides quantitative measures of this improvement. While the overriding conclusion from Table 2 is that the inclusion of ch33 significantly improves the performance, Table 2 also shows that of the three window–only results, the VIIRS climate is the best and performs significantly better for optically thin cirrus compared the four-channel VIIRS channel set. The conclusion from this is that the inclusion of ch20 hurts the performance within the context of the analysis described above. The most likely reason for this is that the large amount of scattering present in this channel is not properly accounted for in the forward model used in this study. Another possible contributing factor is that the Yang database may not be spectrally consistent across the whole of the infrared spectrum. Based on this analysis, the application of the VIIRS climate channel set does not offer any degradation of the cloud-top pressure performance and brings the advantage of day/night consistency. Advances in scattering models and fast forward models will mitigate the uncertainties that arise from using ch20 and may result in improved retrievals in the future.

### 4.3. Comparison of the Optimal Cloud-Top Pressure Solutions

[32] The goal of this study is to examine the impact of the spectral content on the cloud-top pressure solution space, which will influence an algorithm's performance. However, the preceding analysis can be used to generate an optimal cloud-top pressure value defined by where the BTD difference is nearest to zero. This section further explores this approach.

[33] The optimal cloud-top pressure values derived from determining where the BTD differences are near zero are shown as the blue symbols in Figures 11 and 12. In addition, they are also computed for the VIIRS climate channel set shown in Figure 14. Table 3 provides the mean and standard deviation statistics of the optimal cloud-top pressure values relative to the cloud-top pressure values given by CALIPSO/CALIOP. Figure 15 shows the distributions of the cloud-top pressure differences. The mean and standard deviation of the cloud-top pressures from CALIOP for the ice clouds in this scene were 170 hPa and 17 hPa, respectively. For reference, the MYD06 values are also included in Table 3. One obvious feature of Figure 15 is the significant positive bias in the cloud-top pressure from all of the approaches compared to CALIOP. This result is consistent with the expectation that the IR measurements of cloud-top pressure provide the effective level of emission, which tends to occur below the cloud-top pressure but within the actual cloud boundaries. To improve the agreement with CALIPSO, we would need to account for the weighting functions of the IR channels within the cloud used in each solution method [*Holz et al.*, 2006]. Again, the data used are taken from the cirrus shown in Figures 2–4. The relative performance for the VIIRS, GOES-R and VIIRS climate channel sets are the same as they were for

**Table 3.** Comparison of the Mean and Standard Deviation of the Optimal Cloud-Top Pressures Relative to the CALIPSO/CALIOP Cloud-Top Pressure Values

| Channel Set | Bias (hPa) | Standard Deviation (hPa) |
|---|---|---|
| 20, 29, 31, 32 | 104 | 105 |
| 29,31,32 | 56 | 109 |
| 31,32,33 | 31.9 | 59.4 |
| 31,33 ($\beta$ = 1.06) | 30.7 | 74.5 |
| 31,33 ($\beta$ = 1.0) | 8.22 | 77.2 |
| 31,32 ($\beta$ = 1.03) | 33.67 | 89.5 |
| MYD06 | 29.21 | 54.64 |

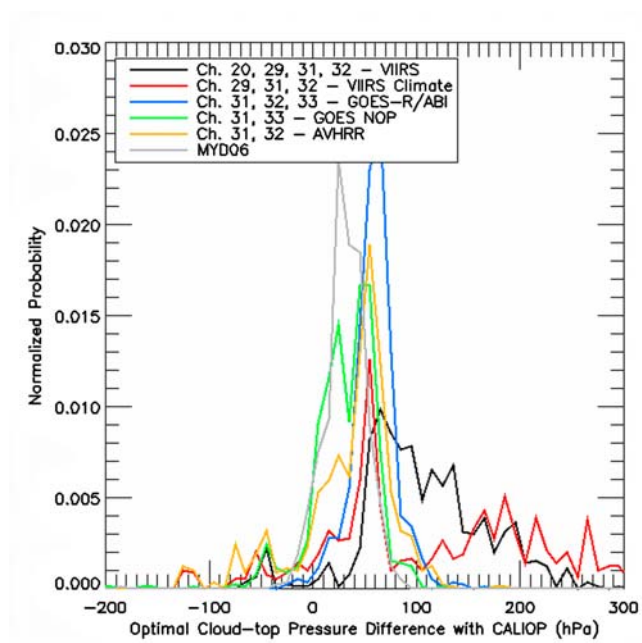


**Figure 15.** Histogram of the optimal cloud-top pressure estimated by the various channel sets relative to cloud-top pressure from CALIPSO/CALIOP for the ice clouds in the cross section shown in Figure 3. Statistics are given in Table 2.

the solution space analysis given in Table 2. The VIIRS channel set generated the largest bias and standard deviation. For example, the GOES-R bias was roughly one half of the value for the VIIRS climate value and almost one third of the value provided by the VIIRS channel set.

### 4.4. Computation of the Cloud-Top Pressure Solution Space for POES/AVHRR and GOES-NOP Imagers

[34] Section 4.3 explored the solution space offered by a three-channel GOES-R/ABI and four-channel NPOESS/VIIRS set of channels. This same analysis can be applied to those imagers that are currently operational and a comparison of the solution spaces spanned by the current POES and GOES operational imagers is provided in this section as a reference. The NESDIS operational GOES-NOP imager cloud height algorithm uses ch31 and ch33 [*Schreiner and Schmit*, 2001]. The NESDIS operational POES/AVHRR cloud height algorithm uses the split-window channels (ch31 and ch32) and is described by *Heidinger and Pavolonis* [2009].

[35] The main strength of the AVHRR data is that it now spans over 3 decades. These results shown here are also relevant to efforts to derive multidecadal climatologies of satellite derived cloud-top pressure. The ability to detect any trend in cloud-top pressure is intimately linked to the depth of the cloud-top solution space offered by the channel set used in estimating cloud-top pressure. As the cloud-top pressure solution space grows, the ability to confidently detect trends in cloud-top pressure diminishes.

[36] Because both of these algorithms use only two channels, a cloud placed at any level that produces valid emissivities will match both observations. Therefore the solution space must be defined differently than the method used above. For a given channel pair, the solution space can be defined as where the $\beta$ profile is based on a reasonable range in particle size. In this section, we define the solution space as the levels where the $\beta$ values fall within the expected range for realistic ice crystal sizes. For this study, we assume that the $\beta$ range is that consistent by a particle radii range from 10 to 100 $\mu$m assuming aggregate particles. While smaller ice crystals are observed [*Kahn et al.*, 2008], the 10 to 100 $\mu$m range is used to represent the expected range for cirrus particle size distributions. Figures 16 and 17 show the variation of the $\beta$(31,32) and $\beta$(31,33) as a function of particle radius assuming an aggregate habit. As Figures 16 and 17 show, the channels used here are insensitive to changes in particle size once the radii exceed 80 $\mu$m. For the $\beta$(31,32), the suggested range in particle size equated to a $\beta$ range of 1.03 to 1.18. For $\beta$(31,33), this particle radius range equated to a $\beta$ range of 1.03 to 1.2.

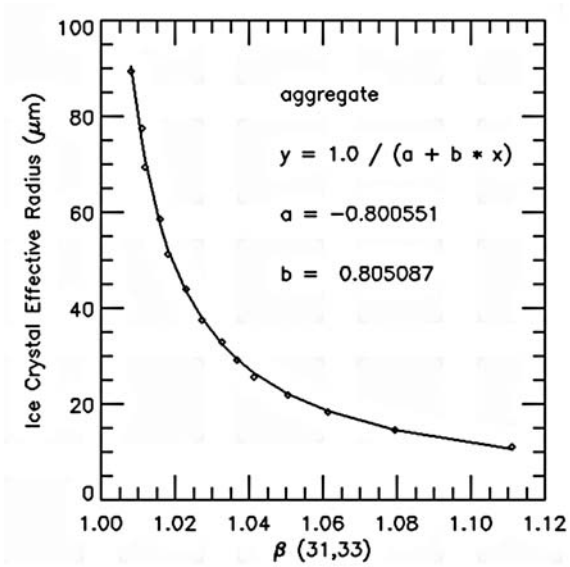


**Figure 17.** Variation of $\beta$(11,13.3) with effective radius for ice crystals modeled as aggregates using the database provided by *Yang et al*. [2005].

[37] Given the expected $\beta$ ranges, we can now define cloud-top pressure solution spaces using the derived $\beta$ profiles. For example, applying the expected $\beta$(31,32) range to the $\beta$(31,32) profile shown in Figure 9 gives a cloud-top pressure space that spans from approximately 150 to 300 hPa. Application of this method to the MODIS-Calipso swath discussed earlier gives the results shown in Figure 18 which

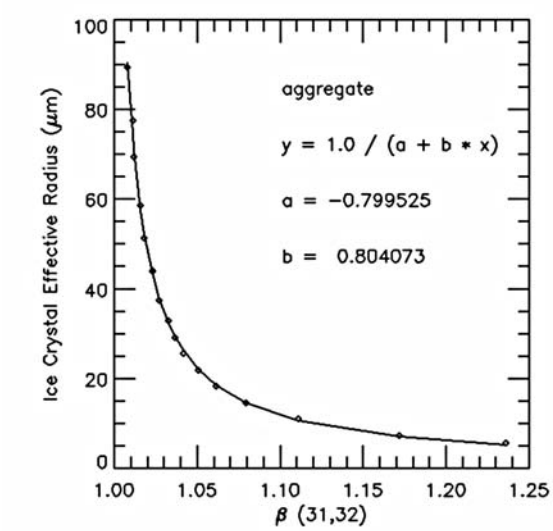


**Figure 16.** Variation of $\beta$(31,32) with effective radius for ice crystals modeled as aggregates using the database provided by *Yang et al*. [2005]. The legend provides the coefficients of a hyperbolic fit.

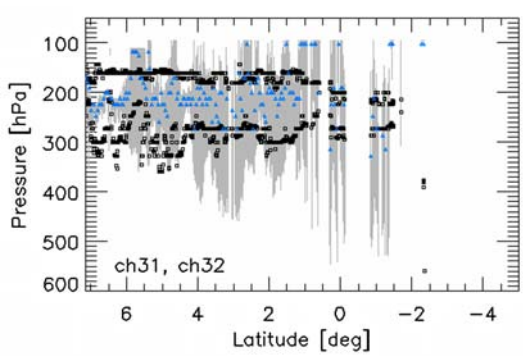


**Figure 18.** Same as Figure 11 but using the POES/AVHRR channel set.

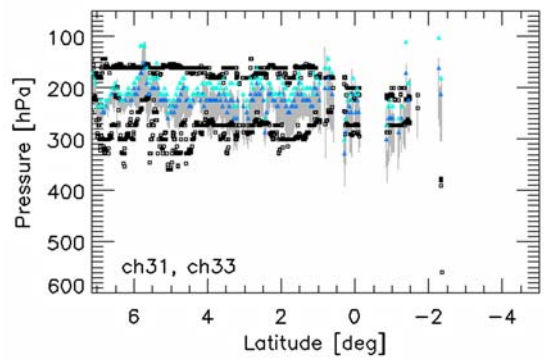


**Figure 19.** Same as Figure 11 but using the GOES-NOP/Image channel set. The light blue points provide the optimal cloud-top pressure solution derived with the assumption that $\beta(31,33) = 1.0$.

are analogous to those shown in Figures 11 and 12. The results of cloud-top pressure solution space provided by ch31 and ch32 appear quite similar to those shown in Figure 11 (chs 20, 29, 31 and 32 aka VIIRS).

[38] Figure 19 shows the results of the application of the $\beta(31,33)$ ranges to the $\beta(31,33)$ profiles for the same case study. Compared to the GOES-R/ABI results shown in Figure 12, there is a noticeable deepening of the cloud-top pressure solution space. This difference in the solution space occurs because of the benefits of the additional cloud microphysical sensitivity offered by ch32 in the GOESR/ABI algorithm. Without this additional channel, an assumption of $\beta(31,33)$ is required to estimate the cloud-top pressure. In the GOES-NOP algorithm, a $\beta(31,33)$ value of 1.0 is always assumed which corresponds to a very large particle radius as shown in Figure 17. Small particle cirrus will therefore produce an overestimation of the cloud-top pressure in the GOES-NOP approach. As Table 2 shows, the cloud-top pressure solution space for the GOES-NOP channels is roughly twice that provided by the GOES-R/ABI except for cirrus with emissivities less than 0.25 where they are approximately equal.

[39] Table 3 provides the results for the optimal cloud-top pressure estimation using the AVHRR and GOES-NOP channel sets. Because each of these channel sets contains only one channel pair, an independent estimate of cloud microphysics is impossible using this analysis. Therefore, an optimal cloud pressure level was defined to be that where the $\beta$ value achieved some predetermined value. In this analysis, the $\beta$ values that defined the optimal solution level were chosen to be those that corresponded to a 30 $\mu$m aggregate crystal. This particular value was chosen since it resulted in a minimal bias with the MYD06 values. As seen in Figures 16 and 17, a 30 $\mu$m aggregate particle produces a $\beta(31,32) = 1.03$ and $\beta(31,33) = 1.06$. The optimal pressure solution from the AVHRR and GOES-NOP is dependent on these values and therefore the bias values should not be compared to those from the other techniques. However, the standard deviations of these values remain meaningful. In terms of the standard deviation of the optimal pressure solution, the GOES-NOP approach gives a value of 75 hPa and the AVHRR solution gives a value of 90hPa. From Figure 3, the actual variation in the cloud-top pressure is much smaller. As expected, both the GOES-NOP and AVHRR standard deviations of the optimal pressure are larger than that provided by the GOES-R and MYD06 values which are less than 60 hPa.

[40] Also shown in Table 3 are the results when the $\beta(31,33) = 1.0$ which corresponds to a true implementation of the GOES-NOP algorithm. It is interesting to note that this $\beta$ value results in the lowest actual bias with CALIPSO. Note that Figure 17 indicates that $\beta(31,33) = 1.0$ is not a valid value for aggregates. Therefore, using $\beta(31,33) = 1.0$ produces an underestimation of the cloud-top pressures, which explains the negative pressure differences regarding the green curve in Figure 15. The agreement between the GOES-NOP and CALIPSO values is therefore fortuitous and is caused by an underestimation of cloud-top pressure that acts to cancel some of the expected overestimation inherent in all IR approaches.

## 5. Conclusions

[41] This paper demonstrates how the availability of specific infrared (IR) channels impacts the ability of two future meteorological satellite imagers to estimate cloud-top pressure. Both of the imagers are planned for launch by the United States, one for a geostationary platform and the other for a polar-orbiting platform. The geostationary imager, the Advanced Baseline Imager (ABI), will be flown first on the GOES-R platform. In addition to the split window channels at 11 and 12 $\mu$m, it has one spectral channel located at 13.3 $\mu$m where there is relatively strong absorption of $H_2O$ and $CO_2$. The polar-orbiting imager, called the Visible Imaging Infrared Radiometer Suite (VIIRS), has spectral channels in window regions only. The lack of an absorbing channel on VIIRS is shown to have negative consequences for the inference of cloud-top pressure. This paper investigates the impact on the ability of a satellite imager such as VIIRS to confidently estimate cloud-top pressure due to the absence of infrared absorption channels. The solution space is defined as the depth of the atmospheric layer in which a cloud can be placed where the calculated top-of-atmosphere radiances match the measurements used in the cloud-top pressure retrieval.

[42] Through an objective analysis applied to MODIS observations, this paper demonstrates the implication of the lack of an absorbing channel on the VIIRS channel selection on the inference of cloud-top pressure. A recurring theme of this paper is that the availability of multiple window channels cannot compensate for the loss of a single absorption channel. This point was examined through a comparison of the cloud-top solution spaces offered by the current POES and GOES imagers. In this comparison, the presence of the absorption channel (ch33) in the GOES-R ABI channel set opposed to the 12 $\mu$m window channel in the POES/AVHRR channel set was shown to offer a significant narrowing of the solution space. For optically thin cirrus, the channels used by the operational VIIRS algorithm provide a solution space of over 200 hPa. However, the inclusion of the single $CO_2$ channel at 13.3 $\mu$m on the GOES-R ABI narrows the solution space to under 30 hPa. Our imager-based analysis is performed using MODIS data, which provides the relevant spectral information with sufficient spatial resolution and radiometric accuracy. Additional results are provided using

data from the current GOES and POES imagers. Active lidar data from CALIPSO/CALIOP observations are used to provide direct measures of the cloud boundaries for verification. Finally, it is shown that a three channel VIIRS channel set that avoids the highly scattering ch20 may offer superior performance without any dependence on solar illumination.

[43] These results shown here are also relevant to efforts to derive multidecadal climatologies of satellite derived cloud-top pressure. The ability to detect any trend in cloud-top pressure is intimately linked to the depth of the cloud-top solution space offered by the channel set used in estimating cloud-top pressure. As the cloud-top pressure solution space grows, the ability to confidently detect trends in cloud-top pressure diminishes.

[44] **Acknowledgments.** The views, opinions, and findings contained in this report are those of the author(s) and should not be construed as an official National Oceanic and Atmospheric Administration or U.S. Government position, policy, or decision. This work was funded primarily by the NOAA Integrated Program Office and by NASA through the Research in Opportunities in Space And Earth Sciences (ROSES) Research Announcement. B.A. Baum is funded through NASA grant NNX08AH04G.

## References

Anderson, G. P., et al. (2000), MODTRAN4: Radiative transfer modeling for remote sensing, *Proc. SPIE Int. Soc. Opt. Eng.*, *3866*, 2–10, doi:10.1117/12.371318.

Baum, B. A., P. Yang, A. J. Heymsfield, S. Platnick, M. D. King, Y.-X. Hu, and S. T. Bedka (2005), Bulk scattering models for the remote sensing of ice clouds. Part 2: Narrowband models, *J. Appl. Meteorol.*, *44*, 1896–1911, doi:10.1175/JAM2309.1.

Bayler, G., R. M. Aune, and W. H. Raymond (2000), NWP cloud initialization using GOES sounder data and improved modeling of nonprecipitating clouds, *Mon. Weather Rev.*, *128*, 3911–3920, doi:10.1175/1520-0493(2001)129<3911:NCIUGS>2.0.CO;2.

Fu, Q., and W. B. Sun (2001), Retrieval of cirrus particle sizes using split-window technique: A sensitivity study, *J. Quant. Spectrosc. Radiat. Transfer*, *70*, 725–736, doi:10.1016/S0022-4073(01)00041-3.

Hannon, S., L. L. Strow, and W. W. McMillan (1996), Atmospheric infrared fast transmittance models: A comparison of two approaches, *Proc. SPIE Int. Soc. Opt. Eng.*, *2830*, 94–105.

Heidinger, A. K., and M. J. Pavolonis (2009) Gazing at cirrus clouds for 25 years through a split-window. Part I: Methodology, *J. Appl. Meteorol. Climatol.*, *48*(6), 1100–1116.

Holz, R. E., S. Ackerman, P. Antonelli, F. Nagle, R. O. Knuteson, M. McGill, D. L. Hlavka, and W. D. Hart (2006), An improvement to the high-spectral resolution $CO_2$-slicing cloud-top altitude retrieval, *J. Atmos. Oceanic Technol.*, *23*(5), 653–670, doi:10.1175/JTECH1877.1.

Jensen, E. J., et al. (2009), On the importance of small ice crystals in tropical anvil cirrus, *Atmos. Chem. Phys.*, *9*, 5519–5537.

Kahn, B. H., C. K. Liang, A. Eldering, Q. Gettelman, Q. Yue, and K. N. Liou (2008), Tropical thin cirrus and relative humidity observed by the Atmospheric Infrared Sounder, *Atmos. Chem. Phys.*, *8*, 1501–1518.

Key, J., D. Santek, C. S. Velden, N. Bormann, J.-N. Thepaut, L. P. Riishojgaard, Y. Zhu, and W. P. Menzel (2003), Cloud-drift and water vapor winds in the polar regions from MODIS, *IEEE Trans. Geosci. Remote Sens.*, *41*(2), 482–492, doi:10.1109/TGRS.2002.808238.

Parol, F., J. Buriez, G. Brogniez, and Y. Fouquart (1991), Information content of AVHRR channels 4 and 5 with respect to the effective radius of cirrus cloud particles, *J. Appl. Meteorol.*, *30*, 973–984.

Schmit, T. J., M. M. Gunshor, W. P. Menzel, J. J. Gurka, J. Li, and A. S. Bachmeier (2005), Introducing the next-generation Advanced Baseline Imager on GOES-R, *Bull. Am. Meteorol. Soc.*, *86*(8), 1079–1096, doi:10.1175/BAMS-86-8-1079.

Schreiner, A. J., and T. J. Schmit (2001), Derived cloud products from the GOES-M imager, paper presented at 11th Conference on Satellite Meteorology and Oceanography, Am. Meteorol. Soc., Madison, WI.

Seemann, S. W., E. E. Borbas, R. O. Knuteson, G. R. Stephenson, and H.-L. Huang (2008), Development of a global infrared land surface emissivity database for application to clear sky sounding retrievals from multispectral satellite radiance measurements, *J. Appl. Meteorol. Climatol.*, *47*(1), 108–123, doi:10.1175/2007JAMC1590.1.

Stephens, G. L., et al. (2002), The CLOUDSAT mission and the A-Train, *Bull. Am. Meteorol. Soc.*, *83*(12), 1771–1790, doi:10.1175/BAMS-83-12-1771.

Wong, E., K. D. Hutchison, S. C. Ou, and K. N. Liou (2007), Cirrus cloud top temperatures retrieved from radiances in the National Polar-Orbiting Operational Environmental Satellite System–Visible Infrared Imager Radiometer Suite 8.55 and 12.0 $\mu$m bandpasses, *Appl. Opt.*, *46*, 1316–1325, doi:10.1364/AO.46.001316.

Yang, P., H. Wei, H.-L. Huang, B. A. Baum, Y. X. Hu, G. W. Kattawar, M. I. Mishchenko, and Q. Fu (2005), Scattering and absorption property database for nonspherical ice particles in the near- through far-infrared spectral region, *Appl. Opt.*, *44*, 5512–5523, doi:10.1364/AO.44.005512.

B. A. Baum, Space Science and Engineering Center, University of Wisconsin-Madison, 1225 W. Dayton St., Madison, WI 53706, USA.

S. Berthier and R. E. Holz, Cooperative Institute for Meteorological Satellite Studies, University of Wisconsin-Madison, 1225 W. Dayton St., Madison, WI 53706, USA.

A. K. Heidinger and M. J. Pavolonis, Center for Satellite Applications and Research, NESDIS, NOAA, 1225 W. Dayton St., Madison, WI 53706, USA. (andrew.heidinger@noaa.gov)